Earth and Planetary Science Letters 616 (2023) 118210

Contents lists available at ScienceDirect

Earth and Planetary Science Letters

journal homepage: www.elsevier.com/locate/epsl

No detectable redox exchange between sulfur and iron during rapid cooling of basalts

Michelle J. Muth *, Elizabeth Cottrell

Department of Mineral Sciences, National Museum of Natural History, Smithsonian Institution, Washington DC 20560, USA

ARTICLE INFO

Article history:
Received 27 October 2022
Received in revised form 25 April 2023
Accepted 3 May 2023
Available online 1 June 2023
Editor: R. Hickey-Vargas

Keywords:
basalts
redox
sulfur
iron

ABSTRACT

The valence states of iron and sulfur in mantle-derived melts influence and respond to the composition of the mantle as well as the subsequent evolution of those melts in Earth's crust. Characterizing the valence states of iron and sulfur in silicate melts that have quenched to form glasses is therefore critical to understanding the composition of the mantle and the magmatic processes that take place before and during volcanic eruptions. Glasses quenched from silicate melts offer the opportunity to precisely measure sulfur and iron valence states, but whether the transition from melt to glass affects the valence state of sulfur and iron is uncertain. Here, we use the glassy margins of two pillow basalts, one from a mid-ocean ridge and one from a back-arc basin, as a natural experiment to test the effect of quench rate on sulfur and iron valence states. We report micro-X-ray Absorption Near Edge Structure (XANES) measurements of $S^{6+}/\Sigma S$ ($S^{6+}/[S^{6+}+S^{2-}]$) and $Fe^{3+}/\Sigma Fe$ ($Fe^{3+}/[Fe^{2+}+Fe^{3+}]$) along transects from the rapidly quenched rims of the pillows down into the slowly cooled crystal-rich interiors. The range of average quench rates estimated for our selected analysis areas range from 1.2×10^5 °C/sec at the pillow margin to 1.1 °C/sec in the interior and span quench rates experienced by natural and experimental glasses. On average, $S^{6+}/\Sigma S = 0.09\pm0.01$ and $Fe^{3+}/\Sigma Fe = 0.147\pm0.002$ in the mid-ocean ridge sample and $S^{6+}/\Sigma S = 0.21\pm0.01$and $Fe^{3+}/\Sigma Fe = 0.153\pm0.004$ in the back-arc sample, where the quoted uncertainty is the 1σ standard deviation of $n=$ 9-16 analyses. We find that the $S^{6+}/\Sigma S$ and $Fe^{3+}/\Sigma Fe$ values along transects in each sample show no systematic changes with depth, and by proxy, no systematic changes with quench rate. In each pillow, all measured $S^{6+}/\Sigma S$ and $Fe^{3+}/\Sigma Fe$ ratios are within the absolute uncertainty of each technique. We propose that these observations are consistent with either sluggish reaction kinetics between sulfur and iron, or an insignificant temperature effect on sulfur-iron redox exchange equilibria. These observations demonstrate that sulfur and iron valence states in glasses with varying quench rates can be directly compared, and that changes in sulfur and iron valence during quench are below the limits of detection with XANES.

1. Introduction

Measuring sulfur and iron valence state, commonly expressed as $S^{6+}/\Sigma S$ and $Fe^{3+}/\Sigma Fe$, in natural and experimentally synthesized basaltic glasses has led to important advances in the understanding of the long-term chemical evolution of Earth's crust and mantle (Bénard et al., 2018; Brounce et al., 2015, 2021; Cottrell and Kelley, 2013; Kelley and Cottrell, 2009; Moussallam et al., 2016, 2019; Muth and Wallace, 2021; Shorttle et al., 2015) and the behavior of magmas before and during volcanic eruptions (Botcharnikov et al., 2011; Brounce et al., 2017; Gennaro et al., 2020; Kelley and Cottrell, 2012; Lerner et al., 2021a; Moussallam et al., 2014a). The redox behaviors of iron and sulfur have the largest impact on the redox-driven behavior of basaltic melts and are closely linked. In addition to driving, or responding to, changes in magma composition due to mantle melting, crystallization, or degassing, these elements can also exchange electrons with each other through the following reaction.

$$S^{2-} + 8Fe^{3+} = S^{6+} + 8Fe^{2+} \quad (1)$$

To interpret measurements of $S^{6+}/\Sigma S$ and $Fe^{3+}/\Sigma Fe$ in silicate glasses, one needs to know if sulfur and iron redox states change to a non-negligible extent as melts cool to form glasses. In other words, we must determine whether any potential sulfur-iron exchange reactions occur at rates comparable to the cooling rates achievable in common laboratory apparatuses and in nature. A quench effect would complicate comparisons between glasses with different cooling rates, and those with different molar proportions

* Corresponding author.
E-mail address: muthm@si.edu (M.J. Muth).

https://doi.org/10.1016/j.epsl.2023.118210
0012-821X/

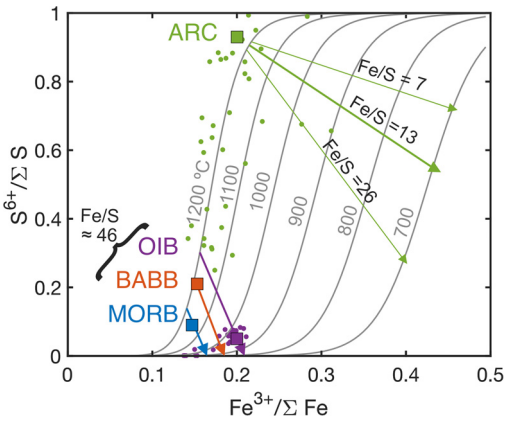

Fig. 1. Modeled cooling paths (colored arrows) of representative basalt compositions from mid-ocean ridges (MORB), back-arc basins (BABB), volcanic arcs (ARC), and ocean islands (OIB) assuming equilibrium sulfur and iron electron exchange occurs throughout the cooling process. Squares show representative measured glass $S^{6+}/\Sigma S$ and $Fe^{3+}/\Sigma Fe$ values (ARC; Muth and Wallace, 2021, OIB; Brounce et al., 2017, BABB; sample TUNE07WT-74D from this study, MORB; sample VG5291 from this study). MORB, BABB, and OIB have similar Fe/S ratios, whereas the higher sulfur content of arc magmas yield lower Fe/S values. Two additional cooling paths are shown for volcanic arcs to demonstrate the effect of molar Fe/S ratio on the redox trajectory. Black equilibrium isotherms and cooling paths calculated using the model of Nash et al. (2019). Measured glass $S^{6+}/\Sigma S$ and $Fe^{3+}/\Sigma Fe$ values in melt inclusions from the southern Cascade arc (green circles; Muth and Wallace, 2021) and submarine glasses from Mauna Kea (purple circles; Brounce et al., 2017, where $Fe^{3+}/\Sigma Fe$ was recalculated using Zhang et al. (2018)) shown for comparison. If electron exchange during quenching of melts to glass occurs as modeled by Nash et al. (2019), then measured $S^{6+}/\Sigma S$ and $Fe^{3+}/\Sigma Fe$ in silicate glasses would not represent magmatic conditions, and measured $Fe^{3+}/\Sigma Fe$ could strongly overestimate melt oxygen fugacity values.

of sulfur and iron concentrations (Métrich et al., 2009) as demonstrated by comparisons between molar Fe/S values shown in Fig. 1.

Quench effects on sulfur and iron valence states have been previously proposed, but there is no consensus on the magnitude or direction of the effects. Métrich et al. (2009) proposed that the reduction of iron and oxidation of sulfur during quench cause a discrepancy between theoretical and observed variations in $S^{6+}/\Sigma S$ as a function of f_{O2} (oxygen fugacity). However, this discrepancy was later found to be an analytical artifact related to beam damage during analysis (Wilke et al., 2008; Jugo et al., 2010). Matjuschkin et al. (2016) suggested that a sulfur species such as S^0, S^{4+} or S_3^- is necessary to explain changes in sulfur solubility as a function of f_{O2} at high (1.0 GPa) pressure, but that these sulfur species may not be stable during quench and therefore may not be detected in silicate glass.

More recently, Nash et al. (2019) used a treatment of available thermodynamic data on iron bearing sulfate, sulfide, and oxide solids to estimate the temperature dependence of S-Fe redox exchange reactions and suggested that the sulfur and iron valence states in silicate glasses are affected by a strong temperature dependence during quench (Fig. 1). O'Neill (2021) expanded this treatment to include reactions between sulfur and Ca, Na, and K in addition to Fe, and this approach yielded a much smaller temperature dependence. For example, whereas the Nash et al. (2019) model predicts that during cooling of an arc magma composition from 1100 to 700 °C as calculated in Fig. 1, $Fe^{3+}/\Sigma Fe$ would increase by ~200% relative to initial values, the model of O'Neill (2021) predicts a change of ~15%. However, a subsequent more detailed thermodynamic model from O'Neill and Mavrogenes (2022) predicts a slightly larger temperature dependence, which would yield a change of ~50%.

The lack of direct observational evidence for or against a quench effect makes these contrasting arguments difficult to reconcile. Previous experiments establishing that iron valence state is preserved during quench (Dyar et al., 1987; Wilke et al., 2002) were conducted on sulfur-free compositions, and therefore cannot be directly applied to the problem at hand. Berry et al. (2003) documented that the electron exchange reaction ($Cr^{2+} + Fe^{3+} = Cr^{3+} + Fe^{2+}$), makes it difficult to quench Cr^{2+} in basaltic glasses, but because Cr is present in trace amounts in most silicate glasses, the related shift in Fe redox state in basaltic melts is likely negligible.

An alternative approach to laboratory experiments is to use the glassy, rapidly quenched margins of pillow basalts as a natural experiment. Pillow rims contain glass that is compositionally homogeneous but that has cooled at rates that vary by orders of magnitude, ranging from the rapidly quenched outer margin to the slowly cooled crystalline interior (Fig. 2, S3). Cottrell and Kelley (2011) demonstrated that in mid-ocean ridge basalt (MORB) pillows, $Fe^{3+}/\Sigma Fe$ values are homogenous throughout all glassy areas of quenched margins. However, because $S^{6+}/\Sigma S$ values were not measured in this study, it was unclear if, similar to Cr^{2+}, S^{6+} was not abundant enough in the melt to affect the valence state of iron.

In this study, we specifically investigate sulfur-iron redox exchange during quench by comparing measurements of $Fe^{3+}/\Sigma Fe$ and $S^{6+}/\Sigma S$ along transects of pillows of MORB and back-arc basin basalt (BABB). By including a back-arc sample with higher $S^{6+}/\Sigma S$, and by measuring $S^{6+}/\Sigma S$ and $Fe^{3+}/\Sigma Fe$ in the same samples, we can more accurately predict any hypothetical quench effect and compare those predictions to measured values. These transects are taken in analysis areas within 100 µm of the pillow-seawater quench contact down to analysis points in glassy pools within the pillows' crystalline interiors. Our analysis areas experienced quench rates that span those found in both naturally and experimentally quenched silicate glasses. We therefore use these pillows as a natural experiment to test the relationship between quench rate and sulfur and iron valence state in basaltic glasses.

2. Methods

2.1. Samples

Sample TUNE07WT-74D is from the WASTUNE-7-074 station from the WASTUNE-7 expedition, in the Northern portion of the Mariana Trough. Sample VG5291 (USNM 115296-3) is from the Central Indian Ridge. Both samples were selected from seafloor pillows with well-preserved palagonite crusts to ensure a complete transect starting from the pillow exterior. In both samples, the glassy areas show no visible signs of devitrification. Samples were prepared as double polished thin sections mounted on Fe-free slides. Sample VG5291 is the same double polished section on which an Fe valence state transect was collected by Cottrell and Kelley (2011). Sample analysis areas are shown in Supplementary Fig. 1 for Sample TUNE07WT-74D and Supplementary Fig. 2 for samples VG5291.

Average cooling rates during quench in each analysis area were calculated following the approach of Cottrell and Kelley (2011) based on a semi-infinite solid with a surface temperature of zero (Carlsaw and Jaegar, 1984) and assuming thermal diffusivity of 0.3 (Hofmeister et al., 2016), initial temperatures of 1200 °C and quench occurring at a glass transition temperature of 725 °C (Cottrell and Kelley, 2011; Ryan and Sammis, 1981). We use average cooling rate values for ease of comparison but note that the instantaneous cooling rates also vary widely along each transect (Fig. S3). Using a thermal diffusivity value for partially crystalline basalt (0.5; Hofmeister et al., 2016) reduce the calculated average cooling rate by ~50-70%. Uncertainty due to complexities in the geometry of the pillow rim (e.g., curved outer surface) are more difficult to determine. As a first order constraint we propagate an uncertainty of ±100 µm through the calculations and find that this also yields a relative of uncertainty of ~50-70%. We therefore estimate the uncertainty on average cooling rates to be roughly 60% but

emphasize that cooling rate should decrease by many orders of magnitude as our analysis area is traversed irrespective of the accuracy of the average cooling rates.

2.2. X-ray absorption near edge structure

$Fe^{3+}/\Sigma Fe$ ratios in TUNE07WT-74D were measured using Fe-XANES at station 13-ID-E at the Advanced Photon Source (APS), Argonne National Laboratory, USA., following the method of Cottrell et al. (2009) modified to mitigate beam damage (Cottrell et al., 2018). Beam damage was mitigated by using 150-200 μm Al foil filter which decreased the beam flux to ~2-4 x 10^9 photons/sec, and by defocussing the beam to approximately 25 × 25 μm. To ensure that these mitigation steps were adequate, we conducted damage tests on a hydrous glass of similar composition and found little to no change over 300 seconds (Fig. S4). Although our damage test only extends to 300 seconds in comparison to the ~11-minute scan used to collect Fe XANES spectra, each scan reaches the peak of the second pre-edge doublet (7113 eV) in 292 seconds. 300 seconds is therefore comparable to time required to scan the pre-edge region during each analysis.

$Fe^{3+}/\Sigma Fe$ values were calculated from the centroid of the pre-edge doublet using a calibration constructed using the basalt standard glasses of Cottrell et al. (2009) and the updated Mössbauer $Fe^{3+}/\Sigma Fe$ values from Zhang et al. (2018), which accounts for recoil-free fraction. The calibration is based on analyses of the standard glasses in October 2022 at APS, where the spectra were processed using the fitting approach described in Lerner et al. (2021b). The same fitting approach is applied to our unknowns here. Use of the Berry et al. (2018) calibration would shift all our $Fe^{3+}/\Sigma Fe$ ratios to systematically lower values but would not change our interpretations. Standard glass LW_0 (Cottrell et al., 2009) was analyzed repeatedly throughout each analytical session, and we corrected pre-edge centroid energies such that the centroid LW_0 ≡ 7112.3 eV. We analyzed only optically clear glass and did not observe any evidence of crystal interference in the spectra. Raw Fe-XANES spectra and calibration details are included in Supplementary Table 3. Reported values are averages of one to five scans in each area within the transect. $Fe^{3+}/\Sigma Fe$ values in MORB pillow VG5291 were calculated based on centroid data reported in Cottrell and Kelley (2011) using the calibration of Zhang et al. (2018).

$S^{6+}/\Sigma S$ values in TUNE07WT-74D and VG5291 were measured using S-XANES at APS following the method outlined in Lerner et al. (2021b). Beam damage was mitigated by lowering the incident beam flux to ~1-70 x 10^9 photons/sec and defocussing the beam to approximately 50 × 50 μm. At these conditions, little to no beam damage is expected to occur (Lerner et al., 2021b). To check that beam damage was negligible, we conducted two ~5-minute scans on each analysis point and checked for consistency between each scan to ensure beam damage had not occurred. We observe no difference between the first and second scan on any of our analyses. Analyses were taken only in optically clear glassy pools. $S^{6+}/\Sigma S$ ratios were calculated using the spectra reduction and peak fitting approach outlined in Lerner et al. (2021b) based on the calibration of Jugo et al. (2010). Reported values are based on one analysis point in each area. Raw S-XANES spectra are included in the supplementary materials.

The measurement precision of $Fe^{3+}/\Sigma Fe$ values, based on three repeat analyses of standard glass LW_0 at the same conditions as those applied to samples described here, is $1\sigma = \pm 0.004$. The overall uncertainty of $Fe^{3+}/\Sigma Fe$ calculated from Fe-XANES spectra, based on a leave-one-out analysis of the calibration of Zhang et al. (2018) is $1\sigma = \pm 0.01$. The measurement precision of $S^{6+}/\Sigma S$ values, based on repeat analyses of standard glass VG-2 at conditions similar to those applied to samples described here, is approximately ten percent relative (Lerner et al., 2021b). The overall uncertainty of $S^{6+}/\Sigma S$ measurements is more difficult to quantify because the calibration is not based on independently measured intermediate $S^{6+}/\Sigma S$ values in basalt, and instead assumes that spectra of mixed valence glasses can be calculated via linear combinations of end-member spectra (i.e., S^{2-} and S^{6+} dominated glasses; Lerner et al., 2021b; Jugo et al., 2010). Our approach yields $S^{6+}/\Sigma S$ values that are offset to lower $S^{6+}/\Sigma S$ values by ≤0.03 compared to values calculated using unscaled S^{2-} and S^{6+} peak areas (e.g., Brounce et al., 2022; Konecke et al., 2019). Other studies apply scaling factors to account for variable beam absorption cross sections in different S chemical species (Manceau and Nagy, 2012; Nash et al., 2019). These scaling factors yield higher $S^{6+}/\Sigma S$ values for a given S-XANES spectra. Muth and Wallace (2021) demonstrate that any error introduced by scaling factor uncertainties is likely small. However, without a suite of glasses analyzed for $S^{6+}/\Sigma S$ with both S-XANES and an independent method, it is difficult to determine which of these approaches is most accurate. In this contribution, we quantify S-XANES calibration uncertainty by using $S^{6+}/\Sigma S$ values calculated with unscaled peak height areas as the lower limit and $S^{6+}/\Sigma S$ values calculated using the scaling factor from Nash et al. (2019) as the upper limit. This approach leads to an asymmetric calibration uncertainty of +0.17 −0.03 for TUNE07WT-74D, and an uncertainty of +0.13 −0.02 for VG5291. Like our choice of $Fe^{3+}/\Sigma Fe$ calibration, our choice of $S^{6+}/\Sigma S$ calibration could result in a systematic offset in $S^{6+}/\Sigma S$ ratio compared to other calibrations but would not affect our interpretations about potential quench effects, which predict relative changes.

2.3. Electron probe micro-analysis

Major elements and sulfur concentrations were measured using Electron Probe Micro-Analysis on the JXA-8530FPlus HyperProbe Electron Probe Microanalyzer at the National Museum of Natural History, Smithsonian Institution. S Kα peak position for sulfur analyses were calculated using $S^{6+}/\Sigma S$ values measured via S-XANES by assuming that the S Kα position relative to S^{2-} and S^{6+} in glass scales linearly with $S^{6+}/\Sigma S$ (Carroll and Rutherford, 1988). Detailed information about analysis conditions and standards are reported in Supplementary Table 2.

2.4. Fourier transform infrared spectroscopy

H_2O concentration in sample TUNE07WT-74D was analyzed on a Thermo Scientific Nicolet 6700 FT-IR spectrometer interfaced with a Continuum IR microscope at the National Museum of Natural History, Smithsonian Institution. H_2O concentrations were calculated from IR peak absorbance values using the Beer-Lambert Law. H_2O concentration was determined using the 3570 cm^{-1} OH^- peak with absorption coefficient $\varepsilon = 63 \pm 3$ from Dixon et al. (1995). Thickness was determined using the interference fringe method (e.g., Wysoczanski and Tani, 2006). Hydrous densities were determined by iteration between calculated glass densities (Luhr, 2001) and Beer-Lambert calculations. H_2O concentration uncertainty as reported in Supplementary Table 1 is based on the propagated uncertainty of thickness in each analysis spot.

3. Results

We reported the 1σ absolute uncertainty on our unknowns in the methods section (±0.01 for $Fe^{3+}/\Sigma Fe$, +0.17 −0.3 for $S^{6+}/\Sigma S$ in sample TUNE07WT-74D, +0.13 −0.2 for $S^{6+}/\Sigma S$ in sample VG5291). Here we report reproducibility, or the 1σ standard deviations from the average of n measurements on a sample. $Fe^{3+}/\Sigma Fe$ in MORB pillow VG5291, recalculated using Zhang et al. (2018) from centroid values reported in Cottrell and Kelley (2011) ranges

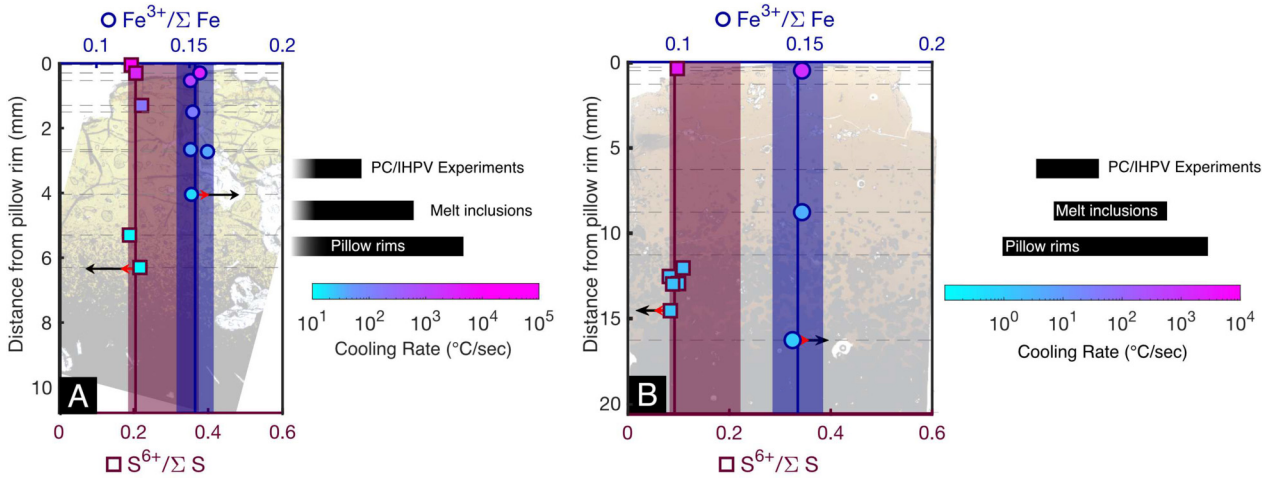

Fig. 2. Fe-XANES (top axis, circle symbols) and S-XANES (bottom axis, square symbols) analyses of (A) back-arc basalt pillow TUNE07WT-74D and (B) MORB pillow VG5291 shown as a function of distance from the pillow rim. Data is overlain on plane polarized images of each sample to show approximate analysis depth. Detailed analysis point locations shown in Supplemental Figs. 1 and 2. Fe-XANES data re-reported from Cottrell and Kelley (2011) for VG5291, but updated to the calibration of Zhang et al. (2018). $Fe^{3+}/\Sigma Fe$ and $S^{6+}/\Sigma S$ show no systematic changes with depth, despite a wide range of cooling rates. For each analysis type, the solid vertical line represents the average value for the sample. The blue and red shaded regions show the calibration uncertainty for unknowns as described in the methods. Symbol interior colors are scaled to average cooling rate during quench calculated based on distance to pillow exterior as described in the section 2.1. These cooling rates are shown in comparison to cooling rate estimates for melt inclusions (Newcombe et al., 2020), glassy pillow lava margins (Helo et al., 2013; Nichols et al., 2009), and experimental apparatuses used to reproduce conditions of upper mantle melting and crustal storage (Piston Cylinder (PC); Bondar et al., 2020, Internally Heated Pressure Vessel (IHPV); Wilke et al., 2002). Black arrows show the magnitude of the expected change in $Fe^{3+}/\Sigma Fe$ and $S^{6+}/\Sigma S$ in slow-cooled portions of the transect assuming a closure temperature of 993 °C according to the model of Nash et al. (2019). Red arrows show the magnitude of expected change calculated using the model of O'Neill and Mavrogenes (2022).

from 0.145 to 0.149, with an average of 0.147±0.002 (n=9) analyses. Measured $S^{6+}/\Sigma S$ ranges from 0.08 to 0.11, with an average of 0.09±0.01 (n=8). Average sulfur and iron concentrations are 728±9 ppm and 7.06±0.13 wt.%, respectively (n=8). Average H_2O concentration as reported in Cottrell and Kelley (2011) is 0.32±0.01 wt.% (n=9). Magmatic temperature calculated using the model of Sugawara (2000) with the hydrous liquidus depression term of Médard and Grove (2008) is 1167±30 °C, where uncertainty is taken from the calibration uncertainty of Sugawara (2000). Average cooling rates for each XANES analysis area, calculated as described in the methods section, range from $3.3\pm1.9\times10^3$ to 1.1±0.8 °C/sec, where uncertainty is 60% relative as described in the methods section. These values correspond to quench times of 0.15 and 357 seconds, respectively.

$Fe^{3+}/\Sigma Fe$ in BABB pillow TUNE07WT-74D ranges from 0.151 to 0.160, with an average of 0.153±0.004 (n=17). $S^{6+}/\Sigma S$ ranges from 0.19 to 0.22, with an average of 0.21±0.01 (n=14). Average sulfur and iron concentrations are 1202±18 ppm and 10.39±0.17 wt.%, respectively (n=8). Average H_2O concentration is 0.99±0.02 wt.% (n=6). Magmatic temperature calculated using the model of Sugawara (2000) with the hydrous liquidus depression term of Médard and Grove (2008) is 1163±30 °C, where uncertainty is taken from the calibration uncertainty of Sugawara (2000). Average cooling rates range from 1.2±0.7x10^5 to 7.5±4.5 °C/sec, where uncertainty is 60% relative as described in the methods section. These values correspond to quench times of 0.004 and 66 seconds, respectively.

In both transects, $S^{6+}/\Sigma S$ and $Fe^{3+}/\Sigma Fe$ values are within absolute uncertainty of the sample average and show no systematic changes with depth (Fig. 2, Supp. Table 1). Cooling rates span those estimated for most melt inclusions and submarine glasses (Newcombe et al., 2020; Nichols et al., 2009; Helo et al., 2013) in addition to piston cylinder (PC) and internally heated pressure vessel (IHPV) experiments (Bondar et al., 2020; Wilke et al., 2002). Glasses quenched from one atmosphere furnaces can be quenched much more rapidly and are likely comparable to the outermost points in the transect presented here but cannot contain significant sulfur unless the experiment is specifically designed for this purpose (e.g., O'Neill and Mavrogenes, 2022).

4. Discussion

4.1. Sulfur and iron valence during quench

The lack of systematic change in $Fe^{3+}/\Sigma Fe$ or $S^{6+}/\Sigma S$ within each transect indicates that modification of $Fe^{3+}/\Sigma Fe$ and $S^{6+}/\Sigma S$ due to redox exchange during cooling is below detection by the methods we employ. There are several possibilities that can explain this observation, and each has a different implication for the interpretation of $Fe^{3+}/\Sigma Fe$ or $S^{6+}/\Sigma S$.

In the following discussion we make the distinction between two processes that are both generally described as quench effects in the literature. $Fe^{3+}/\Sigma Fe$ and $S^{6+}/\Sigma S$ can change during exposure of silicate melt to an external medium such as the atmosphere (Dyar et al., 1987; Helz et al., 2017; Wilke et al., 2002). We see no evidence for this process in our samples, which would almost certainly be reflected in a redox gradient through each pillow rim, given that even glassy scoria samples with long periods of interaction with the atmosphere are not fully equilibrated (Helz et al., 2017). This conclusion is also consistent with experimental observations that redox fronts in sulfur-free glasses are generally sluggish, and that $Fe^{3+}/\Sigma Fe$ remains constant in all but the most slowly quenched melts when exposed to atmosphere (Dyar et al., 1987; Wilke et al., 2002). This process is not the target of our inquiry, and we do not consider it further.

Here, we concern ourselves with the potential shift in iron and sulfur electron exchange equilibrium during cooling (Métrich et al., 2009; Nash et al., 2019). This "quench effect" could occur within melts regardless of exposure to other mediums. This is the process we are focused on and we outline three ways to explain our observations.

The first explanation is that S-Fe exchange equilibria does shift during cooling in basaltic melts, and that even the most rapidly quenched portions remain completely in equilibrium during cooling. If this were the case, measured $Fe^{3+}/\Sigma Fe$ and $S^{6+}/\Sigma S$ values in all glasses represent conditions at or near the glass transition, regardless of quench rate. This is the conceptual model often applied to water speciation in silicate glasses (Behrens, 2020). However, models based on experiments using sulfur-bearing gas buffers

and sulfur concentration measurements (O'Neill and Mavrogenes, 2022) are consistent with those that measure $S^{6+}/\Sigma S$ directly via S-XANES (e.g. Jugo et al., 2010), which suggests that $Fe^{3+}/\Sigma Fe$ and $S^{6+}/\Sigma S$ values in rapidly quenched experimental glasses reflect those in melts at high temperature and not conditions at the glass transition.

To test whether measured values vary with glass transition temperature, we adopt the approach taken to water speciation in melts by Behrens (2020). The analysis areas of our pillow rinds will vary in their glass transition temperatures because glass transition temperature varies as a function of quench rate. For the range of quench rates in glasses studied here, empirical formulations yield temperature differences of ~150 °C (Nichols et al., 2009; Wilding et al., 2000) between the most rapidly and slowly quenched analysis points. Taking the temperature dependence of Nash et al. (2019), for TUNE07WT-74D this would translate to a shift in $Fe^{3+}/\Sigma Fe$ and $S^{6+}/\Sigma S$ of 0.02 and 0.10, respectively. For VG5291 this would translate to a shift in the $Fe^{3+}/\Sigma Fe$ and $S^{6+}/\Sigma S$ of 0.02 and 0.08, respectively. These shifts should be observable based on the analytical precision of the techniques we employed. We do not see systematic variations consistent with these shifts, although a smaller temperature dependence would make these changes more difficult to detect. Therefore, although we cannot definitively rule out the possibility that quenched $Fe^{3+}/\Sigma Fe$ and $S^{6+}/\Sigma S$ values represent conditions at the glass transition, we consider it unlikely based on these comparisons and previous experimental work as discussed.

A second explanation is that S-Fe exchange equilibria does shift strongly with decreasing temperature, but that these reactions are too sluggish to occur on the timescales of melt quenching. If this were the case, then measured $Fe^{3+}/\Sigma Fe$ or $S^{6+}/\Sigma S$ would directly represent uncooled melt $Fe^{3+}/\Sigma Fe$ or $S^{6+}/\Sigma S$. In this study, transect analysis areas include both analysis areas that are almost completely crystal-free and those near large dendritic crystals that likely formed during quench (Faure and Schiano, 2004). It seems unlikely that sulfur-iron redox exchange would be too slow to occur on the same timescales of crystal growth. We therefore find this explanation unsatisfying.

A third explanation requires S-Fe exchange reactions in basaltic melts to have a very small temperature dependence and predicts that silicate glasses maintain $Fe^{3+}/\Sigma Fe$ and $S^{6+}/\Sigma S$ values that are within error of current calibrations during the process of quenching to silicate glass. In this model, changes to S and Fe valence during cooling from magmatic temperatures to 993 °C would be within uncertainty of $Fe^{3+}/\Sigma Fe$ and $S^{6+}/\Sigma S$ values based on S- and Fe-XANES. We propose that the observations in our data set are most consistent with a temperature dependence so small as to be below analytical detection in this study.

We note that this work does not eliminate the need to assess glass samples carefully for the effects of melt inclusion exchange with crystal hosts (Hartley et al., 2017; Humphreys et al., 2022; Lerner et al., 2021a), redox changes during degassing (Brounce et al., 2017; Helz et al., 2017; Kelley and Cottrell, 2012; Moussallam et al., 2014b), and prolonged interaction of melts with the atmosphere (Helz et al., 2017; Lerner et al., 2021a) when applying measurements of $Fe^{3+}/\Sigma Fe$ and $S^{6+}/\Sigma S$ to the interpretation of magmatic systems. Instead, we advise that ruling out the potential effects of quenching will help identify these other processes in natural data sets with much more certainty.

4.2. Consistency with available models

Because sulfur is chemically reactive with many components used to construct solid media experimental assemblies, and sulfur is volatile, highly reactive, and corrosive at one atmosphere, experiments investigating sulfur redox behavior are technically difficult. Experiments are therefore limited. Currently, the most direct constraints on the effect of temperature on S-Fe redox exchange derives from a suite of 1 atmosphere experiments run at variable temperatures and compositions (O'Neill and Mavrogenes, 2022). In contrast, past calibrations relied on experimental series at a single temperature (e.g., Jugo et al., 2010) or extrapolations based on simplified thermodynamic calculations (Nash et al., 2019).

The transects we collected suggest that the temperature dependence of the Fe-S redox exchange reaction is so small as to be below detection at the analytical resolution of Fe- and S-XANES. The model of Nash et al. (2019) does a better job of predicting reasonable magmatic temperatures for these glasses than the model of O'Neill and Mavrogenes (2022) (Fig. 1, S6); however, the Nash et al. (2019) model predicts a strong negative temperature-dependence for reaction 1 that we do not observe, and that is outside of measurement error in this study (Fig. 1, 2). Our data are therefore inconsistent with the model of Nash et al. (2019). The temperature dependence of O'Neill and Mavrogenes (2022) is smaller than that of Nash et al. (2019), and the predicted shifts in $Fe^{3+}/\Sigma Fe$ and $S^{6+}/\Sigma S$ along the transects presented here are shown in Fig. 2, Fig. S5, and discussed below.

To apply the model of O'Neill and Mavrogenes (2022) to our samples, we must calculate f_{O2} from our measured melt $Fe^{3+}/\Sigma Fe$ ratios because the model is cast in terms of melt f_{O2}. This calculation adds to the model's uncertainty because the empirical models that relate melt $Fe^{3+}/\Sigma Fe$ to melt f_{O2} (Cottrell et al., 2021) – such as Kress and Carmichael (1991), Borisov et al. (2018), or O'Neill et al. (2018) – have associated uncertainties (Fig. S5,S6). In our calculations, we do not consider uncertainty in the experimental data used to create the model nor fitting errors in the calibration; this is therefore a minimum estimate of the O'Neill and Mavrogenes (2022) model error. For MORB like compositions, absolute f_{O2} can be calculated from compositional data to ±0.5 log units (Cottrell et al., 2021).

To be conservative in our discussion, we consider the largest predicted effect of cooling on $Fe^{3+}/\Sigma Fe$ and $S^{6+}/\Sigma S$ values given this uncertainty in f_{O2} (Fig. S5) and apply the model to TUNE07WT-74D (Fig. 2a), which is more sulfate-rich than VG5291 and therefore more sensitive to S-Fe redox exchange. The predicted changes in melt $Fe^{3+}/\Sigma Fe$ and $S^{6+}/\Sigma S$ values as the melt cools from 1163 °C to 993 °C are 0.0096 and −0.054, respectively (Fig. 2, S5). In the case of Fe, this change would be outside the reproducibility of our measurements ($1\sigma = \pm 0.004$) but within the uncertainty of the calibration ($1\sigma = \pm 0.01$). In the case of S, this change would be outside the reproducibility of our measurements (10% relative). This change would also be outside of the calibration uncertainty as shown in Fig. 2 and discussed in the methods section. We see no systematic trends in either $Fe^{3+}/\Sigma Fe$ or $S^{6+}/\Sigma S$ that is consistent with the direction of the expected changes with cooling rate (Fig. 2). Therefore, a temperature effect on the order of that predicted by O'Neill and Mavrogenes (2022) may be consistent with our data if the model errors are larger than the minimum errors we estimate here, as discussed above.

In summary, the tests we perform in this paper are consistent with a small temperature dependence of reaction 1 that is equal to or less than that proposed by O'Neill and Mavrogenes (2022). Due to the uncertainty in converting melt $Fe^{3+}/\Sigma Fe$ to f_{O2}, researchers who wish to directly relate melt $S^{6+}/\Sigma S$ and $Fe^{3+}/\Sigma Fe$, may find that semi-empirical calibrations, such as that presented in Muth and Wallace (2021), best suit their needs (Fig. S7). However, we caution that the calibration of Muth and Wallace (2021) is based on a limited suite of data (arc melt inclusions and MORB), and that the temperature dependence of Muth and Wallace (2021) is also based on the thermodynamic of calculations (O'Neill, 2021), which are more comprehensive than those presented in Nash et al.

(2019) but are still not grounded in experimental data of basaltic melts as in O'Neill and Mavrogenes (2022).

5. Conclusions

We use naturally quenched glasses in the rims of pillow basalts to test if $Fe^{3+}/\Sigma Fe$ or $S^{6+}/\Sigma S$ values in silicate melts change during the process of quenching to glass. To accomplish this goal, we conducted S- and Fe-XANES analyses along several points in each pillow rim, grading from the rapidly quenched pillow exterior to the slowly cooled, crystal-rich interior. We find that $Fe^{3+}/\Sigma Fe$ and $S^{6+}/\Sigma S$ show no systematic change with depth, despite the wide range of quench rates experienced by the glass areas selected for analysis. $Fe^{3+}/\Sigma Fe$ and $S^{6+}/\Sigma S$ values in each transect are all within absolute uncertainty of the sample average. We propose that only a small temperature dependence of S-Fe electron exchange equilibria can be consistent with our observations. Regardless of mechanistic interpretations, however, these results clearly establish that $Fe^{3+}/\Sigma Fe$ and $S^{6+}/\Sigma S$ measurements across natural and experimental glasses with different quench rates can be directly compared.

CRediT authorship contribution statement

Michelle Muth: Conceptualization, Analysis, Modelling, Writing – Original Draft. **Elizabeth Cottrell:** Conceptualization, Input on Analysis and Modelling, Writing – Review and Editing.

Declaration of competing interest

The authors declare that they have no known competing financial interests or personal relationships that could have appeared to influence the work reported in this paper.

Data availability

The data used in this paper are attached in the supplemental material

Acknowledgements

We are grateful for two very thoughtful, supportive, and constructive reviews and editorial handling by Rosemary Hickey-Vargas. We thank Tim Gooding, Tim Rose, and Rob Wardell at NMNH, Smithsonian, for lab support. We thank Glenn Macpherson at NMNH, Smithsonian, for assistance collecting high resolution images of sample TUNE07WT-74D. We acknowledge the support of GeoSoilEnviroCARS (The University of Chicago, Sector 13), which is supported by the National Science Foundation—Earth Sciences (EAR—1634415) and Department of Energy-GeoSciences (DE-FG02-94ER14466). This research used resources of the Advanced Photon Source, a U.S. Department of Energy (DOE) Office of Science User Facility operated for the DOE Office of Science by Argonne National Laboratory under Contract No. DE-AC02-06CH11357. We thank University of California San Diego Scripps Institute of Oceanography for providing sample TUNE07WT-74D and Smithsonian National Museum of Natural History for providing sample VG5291 (USNM 115296-3). This study was made possible by a Smithsonian Peter Buck Fellowship to M.M. and a gift of Gary Byerly in memory of Bill Melson.

Appendix A. Supplementary material

Supplementary material related to this article can be found online at https://doi.org/10.1016/j.epsl.2023.118210.

References

Behrens, H., 2020. Water speciation in oxide glasses and melts. Chem. Geol. 558. https://doi.org/10.1016/j.chemgeo.2020.119850.

Bénard, A., Klimm, K., Woodland, A.B., Arculus, R.J., Wilke, M., Botcharnikov, R.E., Shimizu, N., Nebel, O., Rivard, C., Ionov, D.A., 2018. Oxidising agents in sub-arc mantle melts link slab devolatilisation and arc magmas. Nat. Commun. 9 (1). https://doi.org/10.1038/s41467-018-05804-2.

Berry, A.J., Michael Shelley, J.G., Foran, G.J., O'Neil, H.St.C., Scott, D.R., 2003. A furnace design for XANES spectroscopy of silicate melts under controlled oxygen fugacities and temperatures to 1773 K. J. Synchrotron Radiat. 10.

Berry, A.J., Stewart, G.A., O'Neill, H.S.C., Mallmann, G., Mosselmans, J.F.W., 2018. A re-assessment of the oxidation state of iron in MORB glasses. Earth Planet. Sci. Lett. 483, 114–123.

Bondar, D., Fei, H., Withers, A.C., Katsura, T., 2020. A rapid-quench technique for multi-anvil high-pressure-temperature experiments. Rev. Sci. Instrum. 91 (6). https://doi.org/10.1063/5.0005936.

Borisov, A., Behrens, H., Holtz, F., 2018. Ferric/ferrous ratio in silicate melts: a new model for 1 atm data with special emphasis on the effects of melt composition. Contrib. Mineral. Petrol. 173, 98. https://doi.org/10.1007/s00410-018-1524-8.

Botcharnikov, R.E., Linnen, R.L., Wilke, M., Holtz, F., Jugo, P.J., Berndt, J., 2011. High gold concentrations in sulphide-bearing magma under oxidizing conditions. Nat. Geosci. 4 (2), 112–115. https://doi.org/10.1038/ngeo1042.

Brounce, M., Kelley, K.A., Cottrell, E., Reagan, M.K., 2015. Temporal evolution of mantle wedge oxygen fugacity during subduction initiation. Geology 43 (9), 775–778. https://doi.org/10.1130/G36742.1.

Brounce, M., Stolper, E., Eiler, J., 2017. Redox variations in Mauna Kea lavas, the oxygen fugacity of the Hawaiian plume, and the role of volcanic gases in Earth's oxygenation. Proc. Natl. Acad. Sci. USA 114 (34), 8997–9002. https://doi.org/10.1073/pnas.1619527114.

Brounce, M., Reagan, M.K., Kelley, K.A., Cottrell, E., Shimizu, K., Almeev, R., 2021. Covariation of slab tracers, volatiles, and oxidation during subduction initiation. Geochem. Geophys. Geosyst. 22 (6), 1–30. https://doi.org/10.1029/2021GC009823.

Brounce, M., Boyce, J.W., McCubbin, F.M., 2022. Sulfur in apatite from the Nakhla meteorite record a late-stage oxidation event. Earth Planet. Sci. Lett. 595, 117784. https://doi.org/10.1016/j.epsl.2022.117784.

Carlsaw, H.S., Jaegar, J.C., 1984. Conduction of Heat in Solids. Oxford Science Publications.

Carroll, M.R., Rutherford, M.J., 1988. Sulfur speciation in hydrous experimental glasses of varying oxidation-state- results from measured wavelength shifts of sulfur X-rays. Am. Mineral. 73 (7–8), 845–849.

Cottrell, E., Kelley, K.A., 2011. The oxidation state of Fe in MORB glasses and the oxygen fugacity of the upper mantle. Earth Planet. Sci. Lett. 305 (3–4), 270–282. https://doi.org/10.1016/j.epsl.2011.03.014.

Cottrell, E., Kelley, K.A., 2013. Redox heterogeneity in mid-OceanRidge basalts as a functionof mantle source. Science 340 (6138), 1314–1316. https://doi.org/10.1126/science.1235547.

Cottrell, E., Kelley, K.A., Lanzirotti, A., Fischer, R.A., 2009. High-precision determination of iron oxidation state in silicate glasses using XANES. Chem. Geol. 268 (3–4), 167–179. https://doi.org/10.1016/j.chemgeo.2009.08.008.

Cottrell, E., Lanzirotti, A., Mysen, B., Birner, S., Kelley, K.A., Botcharnikov, R.E., Davis, F.A., Newville, M., 2018. A Mössbauer-based XANES calibration for hydrous basalt glasses reveals radiation-induced oxidation of Fe. Am. Mineral. 103 (4), 489–501. https://doi.org/10.2138/am-2018-6268.

Cottrell, E., Birner, S.K., Brounce, M., Davis, F.A., Waters, L.E., Kelley, K.A., 2021. Oxygen fugacity across tectonic settings. In: Magma Redox Geochemistry, pp. 33–61. https://doi.org/10.1002/9781119473206.ch3.

Dyar, D.M., Naney, M.T., Swanson, S.E., 1987. Effects of quench methods on Fe3+/Fe2+ ratios: a Mössbauer and wet-chemical study. Am. Mineral. 72, 792–800.

Dixon, J., Stolper, E.M., Holloway, J.R., 1995. An experimental study of water and carbon dioxide solubilities in mid-ocean ridge basaltic liquids. Part I: Calibration and solubility models. J. Petrol. 36, 1607–1631.

Faure, F., Schiano, P., 2004. Crystal morphologies in pillow basalts: implications for mid-ocean ridge processes. Earth Planet. Sci. Lett. 220 (3–4), 331–344. https://doi.org/10.1016/S0012-821X(04)00057-3.

Gennaro, E., Paonita, A., Iacono-Marziano, G., Moussallam, Y., Pichavant, M., Peters, N., Martel, C., 2020. Sulphur behaviour and redox conditions in etnean magmas during magma differentiation and degassing. J. Petrol. 61 (10). https://doi.org/10.1093/petrology/egaa095.

Hartley, M.E., Shorttle, O., Maclennan, J., Moussallam, Y., Edmonds, M., 2017. Olivine-hosted melt inclusions as an archive of redox heterogeneity in magmatic systems. Earth Planet. Sci. Lett. 479, 192–205. https://doi.org/10.1016/j.epsl.2017.09.029.

Helo, C., Clague, D.A., Dingwell, D.B., Stix, J., 2013. High and highly variable cooling rates during pyroclastic eruptions on Axial Seamount, Juan de Fuca Ridge. J. Volcanol. Geotherm. Res. 253, 54–64. https://doi.org/10.1016/j.jvolgeores.2012.12.004.

Helz, R.T., Cottrell, E., Brounce, M.N., Kelley, K.A., 2017. Olivine-melt relationships and syneruptive redox variations in the 1959 eruption of Kīlauea Volcano as revealed by XANES. J. Volcanol. Geotherm. Res. 333–334, 1–14. https://doi.org/10.1016/j.jvolgeores.2016.12.006.

Hofmeister, A.M., Sehlke, A., Avard, G., Bollasina, A.J., Robert, G., Whittington, A.G., 2016. Transport properties of glassy and Molten lavas as a function of temperature and composition. J. Volcanol. Geotherm. Res. 327, 330–348. https://doi.org/10.1016/j.jvolgeores.2016.08.015.

Humphreys, J., Brounce, M., Walowski, K., 2022. Diffusive equilibration of H_2O and oxygen fugacity in natural olivine-hosted melt inclusions. Earth Planet. Sci. Lett. 584. https://doi.org/10.1016/j.epsl.2022.117409.

Jugo, P.J., Wilke, M., Botcharnikov, R.E., 2010. Sulfur K-edge XANES analysis of natural and synthetic basaltic glasses: implications for S speciation and S content as function of oxygen fugacity. Geochim. Cosmochim. Acta 74 (20), 5926–5938. https://doi.org/10.1016/j.gca.2010.07.022.

Kelley, K.A., Cottrell, E., 2009. Water and the oxidation state of subduction zone magmas. Science 325 (5940), 605–607. https://doi.org/10.1126/science.1174156.

Kelley, K.A., Cottrell, E., 2012. The influence of magmatic differentiation on the oxidation state of Fe in a basaltic arc magma. Earth Planet. Sci. Lett. 329, 109–121. https://doi.org/10.1016/j.epsl.2012.02.010.

Konecke, B.A., Fiege, A., Simon, A.C., Linsler, S., Holtz, F., 2019. An experimental calibration of a sulfur-in-apatite oxybarometer for mafic systems. Geochim. Cosmochim. Acta 265, 242–258. https://doi.org/10.1016/j.gca.2019.08.044.

Kress, V.C., Carmichael, I.S., 1991. The compressibility of silicate liquids containing Fe_2O_3 and the effect of composition, temperature, oxygen fugacity and pressure on their redox states. Contrib. Mineral. Petrol. 108, 82–92.

Lerner, A.H., Wallace, P.J., Shea, T., Mourey, A.J., Kelly, P.J., Nadeau, P.A., Elias, T., Kern, C., Clor, L.E., Gansecki, C., Lee, R.L., Moore, L.R., Werner, C.A., 2021a. The petrologic and degassing behavior of sulfur and other magmatic volatiles from the 2018 eruption of Kīlauea, Hawai'i: melt concentrations, magma storage depths, and magma recycling. Bull. Volcanol. 83 (6). https://doi.org/10.1007/s00445-021-01459-y.

Lerner, A.H., Muth, M.J., Wallace, P.J., Lanzirotti, A., Newville, M., Gaetani, G.A., Chowdhury, P., Dasgupta, R., 2021b. Improving the reliability of Fe- and S-XANES measurements in silicate glasses: correcting beam damage and identifying Fe-oxide nanolites in hydrous and anhydrous melt inclusions. Chem. Geol. 586, 120610. https://doi.org/10.1016/j.chemgeo.2021.120610.

Luhr, J.F., 2001. Glass inclusions and melt volatile contents at Parícutin volcano, Mexico. Contrib. Mineral. Petrol. 142, 261–283. https://doi.org/10.1007/s004100100293.

Manceau, A., Nagy, K.L., 2012. Quantitative analysis of sulfur functional groups in natural organic matter by XANES spectroscopy. Geochim. Cosmochim. Acta 99, 206–223. https://doi.org/10.1016/j.gca.2012.09.033.

Matjuschkin, V., Blundy, J.D., Brooker, R.A., 2016. The effect of pressure on sulphur speciation in mid- to deep-crustal arc magmas and implications for the formation of porphyry copper deposits. Contrib. Mineral. Petrol. 171 (7), 1–25. https://doi.org/10.1007/s00410-016-1274-4.

Médard, E., Grove, T.L., 2008. The effect of H_2O on the olivine liquidus of basaltic melts: experiments and thermodynamic models. Contrib. Mineral. Petrol. 155, 417–432.

Métrich, N., Berry, A.J., O'Neill, H.S.C., Susini, J., 2009. The oxidation state of sulfur in synthetic and natural glasses determined by X-ray absorption spectroscopy. Geochim. Cosmochim. Acta 73 (8), 2382–2399. https://doi.org/10.1016/j.gca.2009.01.025.

Moussallam, Y., Edmonds, M., Scaillet, B., Peters, N., Gennaro, E., Sides, I., Oppenheimer, C., 2016. The impact of degassing on the oxidation state of basaltic magmas: a case study of Kīlauea volcano. Earth Planet. Sci. Lett. 450, 317–325. https://doi.org/10.1016/j.epsl.2016.06.031.

Moussallam, Y., Oppenheimer, C., Scaillet, B., Gaillard, F., Kyle, P., Peters, N., Hartley, M., Berlo, K., Donovan, A., 2014a. Tracking the changing oxidation state of Erebus magmas, from mantle to surface, driven by magma ascent and degassing. Earth Planet. Sci. Lett. 393, 200–209. https://doi.org/10.1016/j.epsl.2014.02.055.

Moussallam, Y., Oppenheimer, C., Scaillet, B., Gaillard, F., Kyle, P., Peters, N., Hartley, M., Berlo, K., Donovan, A., 2014b. Tracking the changing oxidation state of Erebus magmas, from mantle to surface, driven by magma ascent and degassing. Earth Planet. Sci. Lett. 393, 200–209. https://doi.org/10.1016/j.epsl.2014.02.055.

Moussallam, Y., Oppenheimer, C., Scaillet, B., Gaillard, 2019. On the relationship between oxidation state and temperature of volcanic gas emissions. Earth Planet. Sci. Lett. 520, 260–267. https://doi.org/10.1016/j.epsl.2019.05.036.

Muth, M.J., Wallace, P.J., 2021. Slab-derived sulfate generates oxidized basaltic magmas in the southern Cascade arc (California, USA). Geology 49 (10), 1177–1181.

Nash, W.M., Smythe, D.J., Wood, B.J., 2019. Compositional and temperature effects on sulfur speciation and solubility in silicate melts. Earth Planet. Sci. Lett. 507, 187–198. https://doi.org/10.1016/j.epsl.2018.12.006.

Newcombe, M.E., Plank, T., Zhang, Y., Holycross, M., Barth, A., Lloyd, A.S., Ferguson, D., Houghton, B.F., Hauri, E., 2020. Magma pressure-temperature-time paths during mafic explosive eruptions. Front. Earth Sci. 8, 1–22. https://doi.org/10.3389/feart.2020.531911.

Nichols, A.R.L., Potuzak, M., Dingwell, D.B., 2009. Cooling rates of basaltic hyaloclastites and pillow lava glasses from the HSDP2 drill core. Geochim. Cosmochim. Acta 73 (4), 1052–1066. https://doi.org/10.1016/j.gca.2008.11.023.

O'Neill, H.St.C., 2021. Comment on "Compositional and temperature effects on sulfur speciation and solubility in silicate melts" by Nash et al. [Earth Planet. Sci. Lett. 507 (2019) 187–198]. Earth Planet. Sci. Lett. 560, 116843. https://doi.org/10.1016/j.epsl.2021.116843.

O'Neill, H.St.C., Mavrogenes, J.A., 2022. The sulfate capacities of silicate melts. Geochim. Cosmochim. Acta 334, 368–382. https://doi.org/10.1016/j.gca.2022.06.020.

O'Neill, H.St.C., Berry, A.J., Mallmann, G., 2018. The oxidation state of iron in Mid-Ocean Ridge Basaltic (MORB) glasses: implications for their petrogenesis and oxygen fugacities. Earth Planet. Sci. Lett. 504, 152–162.

Ryan, M.P., Sammis, C.G., 1981. The glass transition in basalt. J. Geophys. Res. 86 (B10), 9519–9535. https://doi.org/10.1029/JB086iB10p09519.

Shorttle, O., Moussallam, Y., Hartley, M.E., Maclennan, J., Edmonds, M., Murton, B.J., 2015. Fe-XANES analyses of Reykjanes Ridge basalts: implications for oceanic crust's role in the solid Earth oxygen cycle. Earth Planet. Sci. Lett. 427, 272–285. https://doi.org/10.1016/j.epsl.2015.07.017.

Sugawara, T., 2000. Empirical relationships between temperature, pressure, and MgO content in olivine and pyroxene saturated liquid. J. Geophys. Res., Solid Earth 105 (B4), 8457–8472.

Wilding, M., Dingwell, D., Batiza, R., Wilson, L., 2000. Cooling Rates of Hyaloclastites: Applications of Relaxation Geospeedometry to Undersea Volcanic Deposits, vol. 61. Springer-Verlag.

Wilke, M., Behrens, H., Burkhard, D.J.M., Rossano, S., 2002. The oxidation state of iron in silicic melt at 500 MPa water pressure. Chem. Geol. 189, 55–67.

Wilke, M., Jugo, P.J., Klimm, K., Susini, J., Botcharnikov, R., Kohn, S.C., Janousch, M., 2008. The origin of S^{4+} detected in silicate glasses by XANES. Am. Mineral. 93 (1), 235–240. https://doi.org/10.2138/am.2008.2765.

Wysoczanski, R., Tani, K., 2006. Spectroscopic FTIR imaging of water species in silicic volcanic glasses and melt inclusions: an example from the Izu-Bonin arc. J. Volcanol. Geotherm. Res. 156, 302–314. https://doi.org/10.1016/j.jvolgeores.2006.03.024.

Zhang, H.L.L., Cottrell, E., Solheid, P.A., Kelley, K.A., Hirschmann, M.M., 2018. Determination of $Fe^{3+}/\Sigma Fe$ of XANES basaltic glass standards by Mössbauer spectroscopy and its application to the oxidation state of iron in MORB. Chem. Geol. 485, 113. https://doi.org/10.1016/j.chemgeo.2018.03.025.